J Mater Sci (2018) 53:13390–13399

Mechanochemical Synthesis

Synthesis, characterization and in situ monitoring of the mechanochemical reaction process of two manganese(II)-phosphonates with N-containing ligands

Irina Akhmetova[1], Konstantin Schutjajew[2], Manuel Wilke[3], Ana Buzanich[1], Klaus Rademann[4], Christina Roth[2], and Franziska Emmerling[1,*]

[1] Federal Institute for Materials Research and Testing (BAM), Richard-Willstaetter-Str. 11, 12489 Berlin, Germany
[2] Institute for Chemistry and Biochemistry, Freie Universität Berlin, Takustr. 3, 14195 Berlin, Germany
[3] Swiss Light Source, Material Science Beamline, Paul Scherrer Institute (PSI), 5232 Villigen, Switzerland
[4] Department of Chemistry, Humboldt-Universität zu Berlin, Brook-Taylor-Str. 2, 12489 Berlin, Germany

Received: 15 February 2018
Accepted: 15 June 2018
Published online: 27 June 2018

ABSTRACT

Two divalent manganese aminophosphonates, manganese mono(nitrilotrimethylphosphonate) ($MnNP_3$) and manganese bis(*N*-(carboxymethyl)iminodi(methylphosphonate)) ($Mn(NP_2AH)_2$), have been prepared by mechanochemical synthesis and characterized by powder X-ray diffraction (PXRD). The structure of the novel compound $Mn(NP_2AH)_2$ was determined from PXRD data. $MnNP_3$ as well as $Mn(NP_2AH)_2$ exhibits a chain-like structure. In both cases, the manganese atom is coordinated by six oxygen atoms in a distorted octahedron. The local coordination around Mn was further characterized by extended X-ray absorption fine structure. The synthesis process was followed in situ by synchrotron X-ray diffraction revealing a three-step reaction mechanism. The as-prepared manganese(II) phosphonates were calcined on air. All samples were successfully tested for their suitability as catalyst material in the oxygen evolution reaction.

Introduction

The chemistry of metal phosphonates has gained importance during the last few decades. As a linker, the phosphono-group is able to coordinate several metal ions in a variety of coordination modes [1]. As a result, metal phosphonates occur in different structures, depending on the nature of the phosphonic acid [2–4]. Metal phosphonates are promising candidates for various applications including gas storage [5, 6], proton conduction [7, 8] and catalysis [9]. Especially transition metal phosphonates are possible (pre)catalysts for oxygen evolution reaction in water electrolysis [10–12]. Typically, metal phosphonates are synthesized in hydrothermal reactions [13]. Here, we present

Address correspondence to E-mail: franziska.emmerling@bam.de

https://doi.org/10.1007/s10853-018-2608-6

mechanochemistry as an efficient and sustainable alternative to the classical solution synthesis. To gain insight in the reaction pathways, in situ methods were recently developed, monitoring mechanochemical reactions in real time by synchrotron XRD and/or Raman spectroscopy [14–16]. Here, we present the synthesis of two Mn(II)-phosphonates with different organic ligands (Scheme 1). The manganese mono(nitrilo-trimethylphosphonate) $MnNP_3$ (**1**) is a known compound and has been synthesized in a hydrothermal reaction by Clearfield et al. [17]. Compound (**2**), a manganese(II)-complex including *N*,*N*-bis(phosphonomethyl)glycine as a ligand could be structurally characterized for the first time. The structure of (**2**) was determined from powder X-ray diffraction (PXRD) data. The formation of both compounds was investigated in situ, and a possible mechanism for the synthesis of both compounds is proposed.

Furthermore, both compounds were calcinated to gain N-, P- and Mn-doped carbon black. EXAFS spectra of the starting compounds and of the calcinated species were collected, so information about the structural changes in the environment of the Mn-atom due to calcination could be acquired. Both Mn samples are applicable in the electrocatalysis of the oxygen evolution reaction (OER) and thus promising non-noble metal alternatives to the commercially applied catalysts in water electrolysis. Preliminary results in alkaline media before and after the samples' calcination are presented.

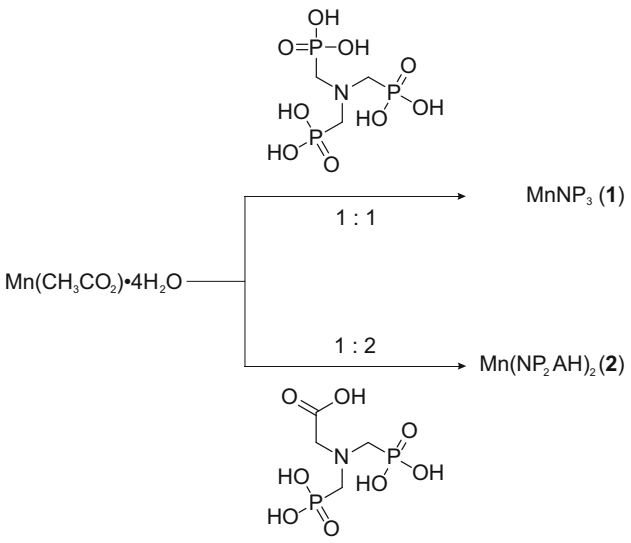

Scheme 1 Reaction scheme for the synthesis of the compounds (**1**) and (**2**).

Experimental section

Chemicals

The following chemicals were used without further purification: manganese(II) acetate tetrahydrate (≥ 99.0%, Fluka Analytical), nitrilotri(methylphosphonic acid) (≥ 97.0%, Sigma Aldrich), *N*,*N*-bis(phosphonomethyl)glycine (≥ 98.0%, Sigma Aldrich).

Synthesis of $MnNP_3$ (1)

The synthesis was performed in a vibrational ball mill (Pulverisette 23, Fritsch, Germany). Manganese acetate tetrahydrate (270.3 mg, 1.10 mmol) and nitrilotri(methylphosphonic acid) (329.7 mg, 1.10 mmol) were added into a stainless steel jar (V = 10 mL). 200 µL of water was added. The grinding was performed at 50 Hz for 15 min using two stainless steel balls ($Ø$ = 10 mm, m = 1.0 g). The damp product was dried in air to obtain a white powder.

Synthesis of $Mn(NP_2AH)_2$ (2)

Manganese acetate tetrahydrate (190.7 mg, 0.78 mmol), *N*,*N*-bis(phosphonomethyl)glycine (409.3 mg, 1.56 mmol) and 200 µL of water were added into a stainless steel vessel. The grinding was performed under the same conditions as for compound (**1**). The gray damp product was dried in air, and a light gray powder was obtained.

Analytical techniques

The powdery reaction products were characterized by PXRD. The samples were measured in transmission geometry mode at a D8 diffractometer (Bruker AXS, Germany) using Cu $K_{\alpha 1}$ radiation. The patterns were collected in a 2θ range from 5° to 60° with a step size of 0.008°. For the structure solution of (**2**), the time per step was increased to 8 s. The indexing was performed with the TOPAS software [18]. Afterward, the structure was solved using the simulated annealing procedure implemented in DASH [19]. The final Rietveld refinement was carried out in TOPAS. The in situ investigations of the reaction process were carried out at the synchrotron Bessy II (Helmholtz Centre for Materials and Energy, Germany). An

adjusted vibrational ball mill and custom-made Perspex jars (V = 10 mL) were used. The details of the experimental setup have been described previously [16]. The milling conditions remained unchanged. The detection was carried out by a two-dimensional MarMosaicCCD detector. The EXAFS (extended X-ray absorption fine structure) spectroscopy measurements were performed at the BAM*line* (Bessy II, Helmholtz-Zentrum Berlin, Germany) [20]. The beam was monochromatized using a double-crystal monochromator (DCM). The X-ray beam size was 5 mm × 1 mm. The measurements were performed at the respective K edge (Mn: 6539 eV) in transmission mode. The excitation energy was varied from 6481 to 7084 eV, with a 0.5 eV energy step width in the near-edge region and 0.04 Å for the k-space in the EXAFS region. To obtain a proper sample thickness, the analyzed substances were mixed with boron nitride and fixed in plastic sample holders. EXAFS data were processed by using ATHENA and ARTEMIS. These GUI programs belong to the main package IFEFFIT (v. 1.2.11) [21]. The $MnNP_3$ and $Mn(NP_2AH)_2$ phases were theoretically modeled and fitted to the measured spectra, respectively, using ARTEMIS. Electrochemical testing of the two samples was carried out in a cyclic voltammetry (CV) experiment, employing a three-electrode aqueous electrochemical cell using a Pt-mesh as the counter and silver chloride electrode (sat. KCl) as the reference and an RDE as the working electrode. As electrolyte, 50 mL of 0.1 M KOH (Fisher scientific, analytical reagent grade) was used at room temperature and purged with N_2 for at least 10 min before each measurement. The working electrode was prepared by adding 10 µL of an ink onto a glassy carbon disk. The ink was prepared via grinding of 2 mg of the catalyst together with 4 mg of carbon black (Vulcan XC 72, Cabot) to ensure suitable electronic conductivity. The mixture was then dispersed in the ink base, which consists of an equivoluminal solution of water (MilliQ®, 18.2 MΩ) and dimethylformamide (DMF, Acros Organics, analytical reagent grade) with 0.7 vol% Nafion (DuPont D2021), using a sonotrode to form a homogenous ink. The ink was pasted on a GC disk and left to dry into a uniform film. Such prepared working electrode was rotated at 1600 rpm, while scanning the potential from 0 to 1 V versus reference with a scan rate of 20 mV/s. The activity of the materials for catalyzing the OER was investigated after a conditioning step, in which the electrode was cycled between − 0.6 and 0.6 V versus reference for 20 cycles. The performance of the catalyst was compared to that of ruthenium(IV)-oxide with the same mass loading on the electrode tip.

Results and discussion

Syntheses and structure characterization

Both manganese phosphonates were synthesized by liquid-assisted grinding. A quantitative conversion of the starting materials is indicated by the absence of the respective reflections in the diffractograms of the products. The formation of (**1**) was verified by comparing the obtained PXRD pattern with the calculated pattern from the known structure (Fig. 1). The structure of (**2**) was solved from PXRD data. The parameters of the unit cells are summarized in Table 1.

Structure of $MnNP_3$ (1)

Compound (**1**) is a coordination polymer consisting of one-dimensional chains [17]. The crystal structure is isomorphic to the analogous Co-containing compound synthesized and characterized by Guan and Wang [22] and is shown in Fig. 2a along the b-axis. The manganese ion is surrounded by six oxygen atoms in a distorted octahedron. The coordination polyhedron is shown in Fig. 2b. Three of the oxygen atoms are provided by three phosphono-groups from two ligands. One of the ligands is twofold

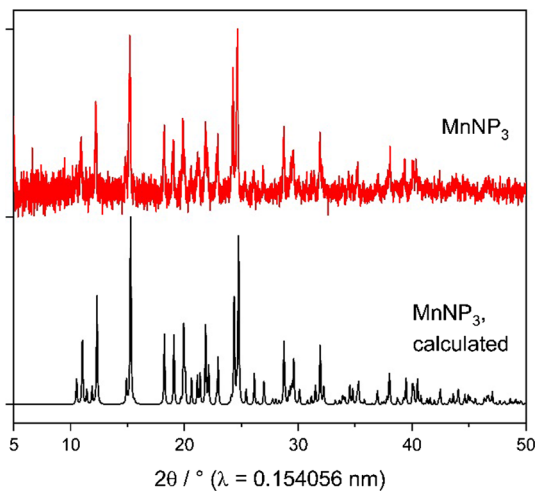

Figure 1 Obtained and calculated XRD patterns for compound (**1**).

Table 1 Crystal data of the compounds $MnNP_3$ (**1**) and $Mn(NP_2AH)_2$ (**2**)

	$MnNP_3$		$Mn(NP_2AH)_2$
Chemical formula	$Mn[HN(CH_2PO_3H)_3(H_2O)_3]$		$Mn[(HO_2CH_2C)NH(CH_2PO_3H)_2]_2$ * $2H_2O$
Crystal system	Monoclinic		Triclinic
	Calculated [17]	Obtained	
Space group	$P2_1/c$	$P2_1/c$	$P\bar{1}$
V (Å^3)	1315.75	1318.29	552.806
a (Å)	9.2834	9.2846	5.58906(11)
b (Å)	16.027	16.0685	10.6986(3)
c (Å)	9.7742	10.1939	9.6342(3)
α (°)			103.310(2)
β (°)	115.209	119.91	80.652(2)
γ (°)			94.122(2)
R_{wp}			3.30
R_{Bragg}			1.07
GOF			2.57

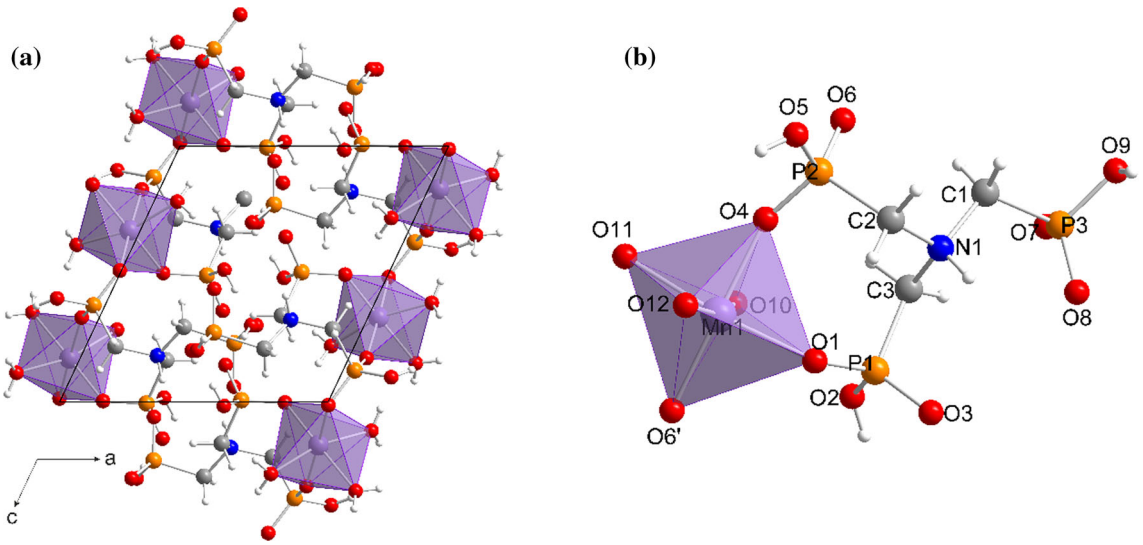

Figure 2 **a** Crystal structure and **b** coordination polyhedron for Mn^{2+} in $MnNP_3$. Violet: manganese, orange: phosphorus, red: oxygen, blue: nitrogen, gray: carbon, light gray: hydrogen.

coordinated on the metal ion. Three water molecules complete the coordination sphere. The single MnO_6-octahedra are interconnected in two ways. A short connection arises from a single phosphono-group coordinating with two oxygen atoms to two different metal ions. The second connection is built with two phosphono-groups of the same ligand bound to two different metal ions. Accordingly, the ligand is bound in η^3-μ_2-coordination mode.

Structure of $Mn(NP_2AH)_2$ (2)

The crystal structure of (**2**) was determined from powder X-ray data and is depicted in Fig. 3a along the *c* axis. The final Rietveld refinement is shown in Fig. 4. $Mn(NP_2AH)_2$ crystallizes in the space group $P\bar{1}$. The parameters of the unit cell can be found in Table 1. The stoichiometry of the compound is 1:2, namely there are two ligand molecules per metal ion. The ligand exists as zwitterion: Both phosphono-groups are deprotonated, while the N-atom is protonated. The Mn^{2+} ion is coordinated by six oxygen atoms in a distorted octahedron. All oxygen atoms

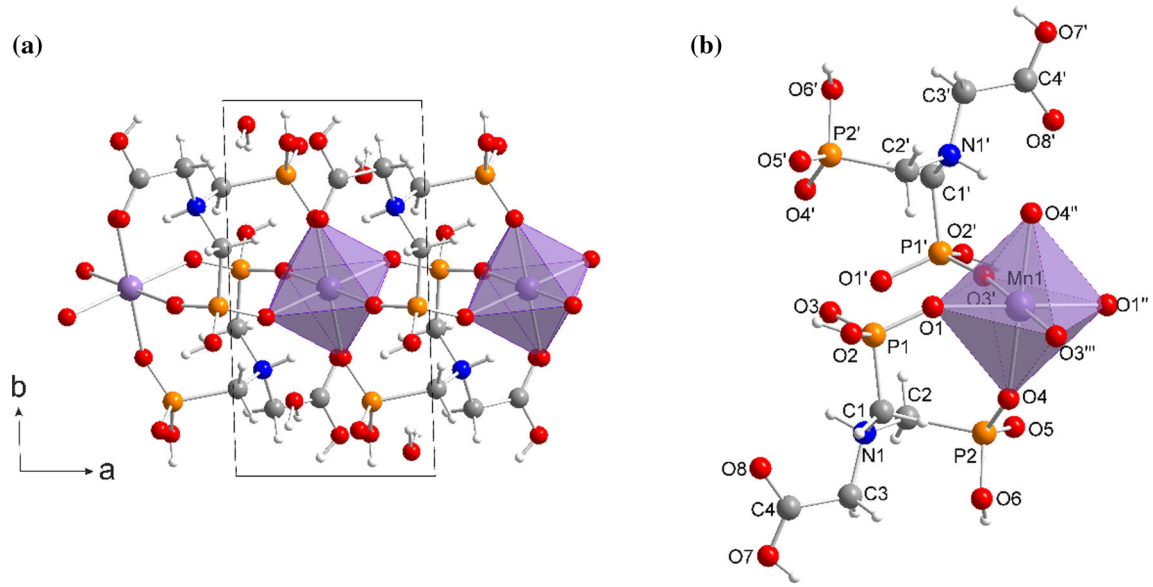

Figure 3 **a** Crystal structure and **b** coordination polyhedron for Mn^{2+} in $Mn(NP_2AH)_2$. Violet: manganese, orange: phosphorus, red: oxygen, blue: nitrogen, gray: carbon, light gray: hydrogen.

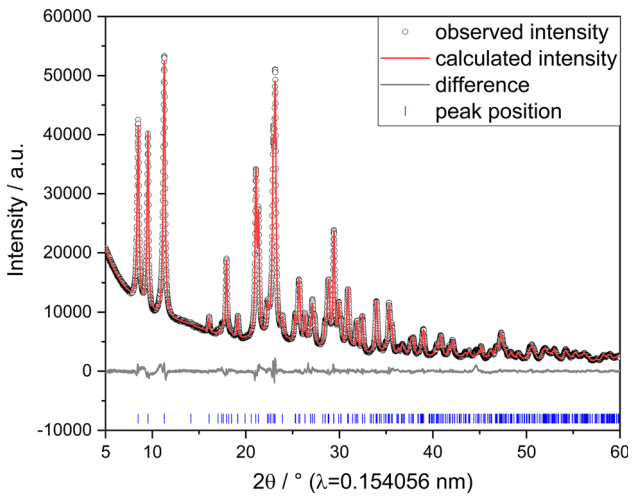

Figure 4 Rietveld refinement for the structure of (**2**). The intensity of the scattered X-ray beam (black circles), the calculated intensity (red line), the difference between measured and calculated intensities (gray line) and the positions of the peak.

are provided by phosphono-groups of the ligand, and the carboxy-group is protonated and not participating in the coordination. Two phosphono-groups of two different ligands connect the octahedra in the center plane, whereby eight-membered rings between the metal ions are formed. Additionally, both ligands chelate the metal centers at their vertices, resulting in Mn1–O1–P1–C1–N1–C2–P2–O4 rings. This type of connection occurs only in one direction. Consequently, the structure consists of one-dimensional chains.

In situ studies

The syntheses were investigated in situ by synchrotron XRD. For this purpose, the syntheses were carried out in a Perspex jar without altering the reaction conditions. The same products were formed as in the steel jar. The whole reaction process can be subdivided into three steps. The 2D plot of XRD patterns for the formation of (**1**) is presented in Fig. 5a. The reflections of the starting materials can be detected during the first 90s of the milling process (step 1). The reflections vanish and introduce a short reaction step characterized by the absence of crystalline materials (step 2). After an overall milling time of 2 min, reflections at $2\theta = 15.2°$, 24.4° and 24.8° appear, indicating the formation of the product (**1**). In Fig. 5b, the 2D plot of the XRD patterns collected during the synthesis of (**2**) is depicted. The initial reflections belonging to the starting materials disappear after 30s of milling (step 1). For the next 6 min, no reflections can be detected. The second step of the reaction does not include crystalline phases. The final step begins at 6.30 min and is characterized by reflections at $2\theta = 8.4°$ and 11.2°, indicating the formation of the product (**2**). These reflections belong to the carboxy- and phosphono-groups of the ligand being pre-ordered. Additional product reflections at

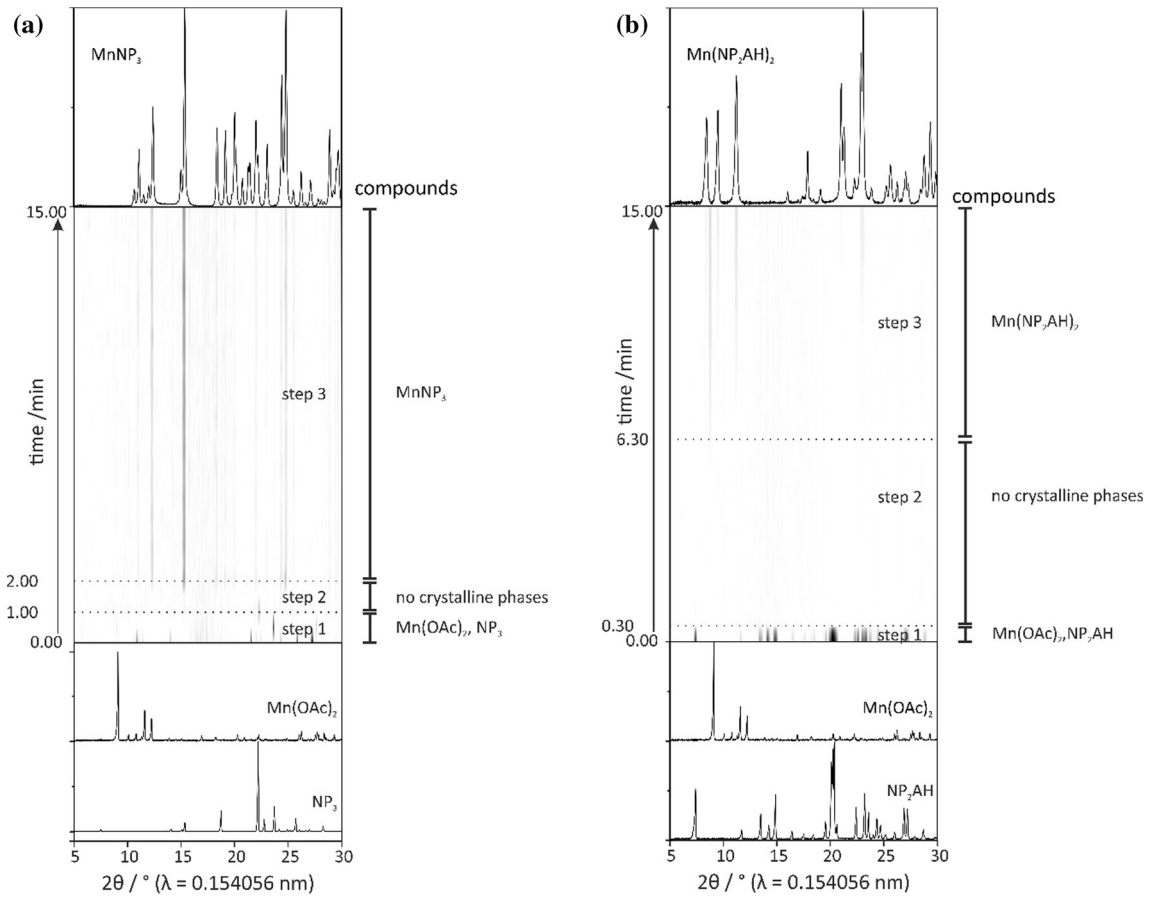

Figure 5 2D plot of the synchrotron XRD data **a** for the synthesis of (**1**) and **b** for the synthesis of (**2**). $Mn(OAc)_2$—manganese(II) acetate tetrahydrate, NP_3—nitrilotri(methylphosphonic acid), NP_2AH—*N*,*N*-Bis(phosphonomethyl)glycine.

2θ = 21.0° and 22.9° occur later during the third step. These reflections arise from the atomic planes built by oxygen atoms from the MnO_6-octahedra. For that reason, it can be assumed that the ligand molecules are reordered before the metal center is bound and the final product becomes completely crystalline.

Thermal treatment

EXAFS measurements were performed to validate the coordination environment around the manganese ions. The EXAFS spectra are shown in Fig. 6 in magnitude and real space, and the fit parameters are summarized in Table 2.

For the manganese nitrilotri(methylphosphonate) (**1**), a coordination number (CN) of 5–6 is observed (Fig. 6, upper row) at the first shell. This is also confirmed by the simulated scattering paths at distances between 2.12 and 2.23 Å (Table 2). For compound (**2**), a CN of 6 can be found (Fig. 6, lower row) at the first shell. This is also confirmed by the simulated scattering path (Mn–O) at a distance of 2.18 Å (Table 2). The second coordination shell could be fitted in good agreement with the simulation as well. A coordination number of 2 is observed (Fig. 6, lower row), which is confirmed by the simulated scattering path (Mn–P) at a distance of 3.6 Å.

The EXAFS spectra are consistent with the crystal structure of the compounds containing Mn atoms in octahedral environment of 6 oxygen atoms. The analyzed samples were calcinated under 600 °C for 1 h. The corresponding DTA/TG curves are shown in Fig. S1. For the measurements, an open Al_2O_3 jar was used. The temperature was increased with a heating rate of 10 K min^{-1}. The heating first leads to the loss of water molecules as an endothermic effect. Later, the combustion of the organic fraction is visible as an exothermic process. In Fig. 7, EXAFS spectra of both substances prior and after calcinations are presented. The coordination number at the first shell decreases to 4 for both samples. Furthermore, the connection

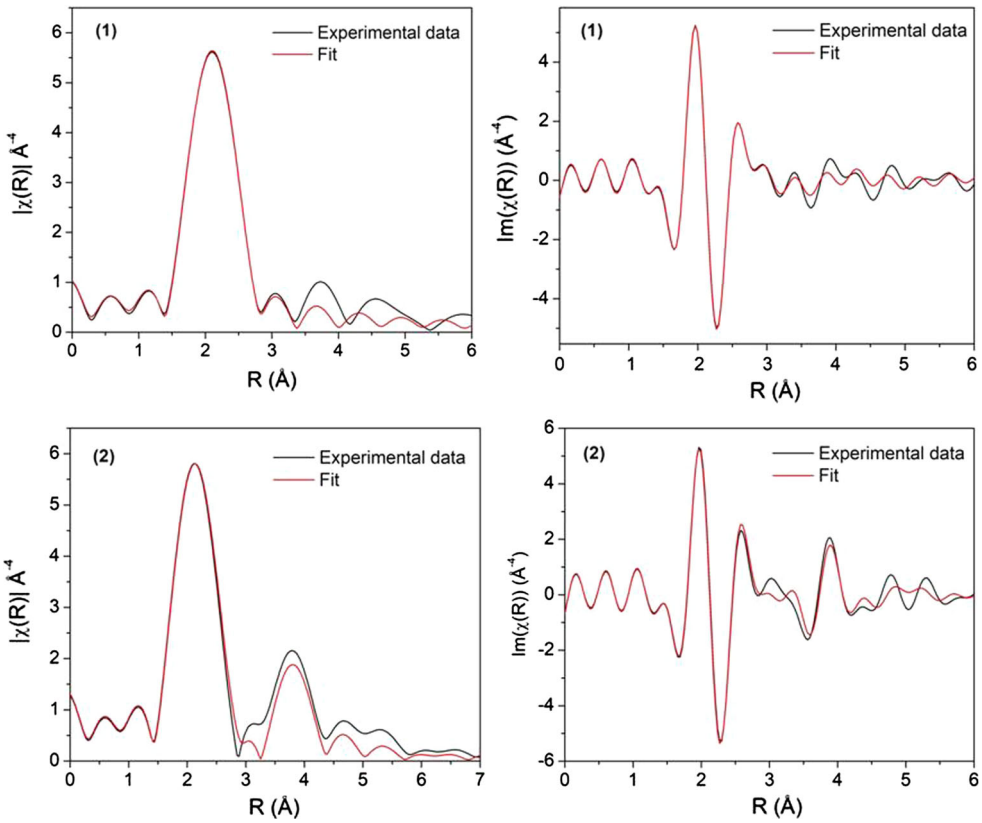

Figure 6 Mn K-edge EXAFS data shown in both magnitude and real space for compounds: (**1**) $MnNP_3$ (**1**) and (**2**) $Mn(NP_2AH)_2$ (**2**).

Mn–P at the second coordination shell of compound **2** vanishes, so the EXAFS data indicate changes in the crystal structure. The XRD patterns of the calcinated species strongly differ from the powder patterns of the pure compounds. In both cases, no reflections of the products can be seen in the XRD after the calcination, indicating the complete dissipation of the original crystal structure (Fig. S2). New crystalline structures are built due to high temperature. The XRD patterns of the calcinated compounds are characterized by a prominent reflection at 9.2° 2θ. The PXRD data for the calcinated (**2**) are determined by amorphous contributions. Few reflections denote the presence of also crystalline phases in the mixture. It is assumed that the new crystalline phases are different manganese oxides. The calcinated products are under further investigations. The potential of both materials in their uncalcinated as well as calcinated state for catalyzing the oxygen evolution reaction (OER) was assessed using a standard electrochemical approach. Commercially available water electrolyzers still rely on expensive noble metals (e.g., iridium). That is why recent research focusses on finding more earth-abundant alternatives to substitute them, in particular in the rather sluggish oxygen reaction. Only recently, Melder et al. [23] reported on the suitability of different MnO_x/C samples for OER electrocatalysis. Figure 8 shows voltammograms of both Mn samples in their pristine and calcinated state measured in alkaline electrolyte. The activity of the samples toward the OER is evident from cyclic voltammetry measurements, even though the overpotential is significantly higher than that of ruthenium(IV)-oxide, which was measured in identical conditions as a standard material. While the onset of oxygen evolution for this standard is already at 0.5 V versus Ag/AgCl, for the Mn samples the current density increases significantly only after 0.65 V versus Ag/AgCl (Fig. 8a). Thermal treatment tends to enhance the overall performance of the catalyst, measured by the apparent current density, which, e.g., for $MnNP_3$, increases from 4 mA/cm^2 first cycle to more than 8 mA/cm^2. However, the activity declines constantly with every consecutive cycle and—after the tenth cycle—is by several times smaller than in the first cycle. It is noteworthy that the choice of the respective pristine Mn seems to have only a negligible influence on its OER activity.

Table 2 EXAFS fit parameters of **1** and **2**

Sample	Scattering path	N	R_{model} (Å)	R_{fit} (Å)	R^2_{diff} (Å)	RMSE (Å)
(1)	Mn–O4	2	2.124	2.070	0.002916	0.303
	Mn–O12	1	2.168	2.113	0.003025	
	Mn–O1	2	2.209	2.155	0.002916	
	Mn–O10	1	2.236	2.182	0.002916	
	Mn–H16	2	2.659	2.604	0.003025	
	Mn–H15	3	2.720	2.666	0.002916	
	Mn–P2	1	2.247	3.192	0.893025	
	Mn–P1	1	3.313	3.258	0.003025	
	Mn–O6–P2	2	3.442	3.387	0.003025	
	Mn–O4	1	3.443	3.388	0.003025	
(2)	Mn–O18.1	6	2.1818	2.20716	0.00064313	0.02536
	Mn–P12.1	2	3.4372	3.46256	0.00064313	
	Mn–P7.1	2	3.5404	3.56576	0.00064313	
	Mn–O19.1–P12.1	4	3.5629	3.58826	0.00064313	
	Mn–P7.2	2	3.6086	3.63396	0.00064313	
	Mn–O16.1–P7.1	4	3.6111	3.63646	0.00064313	
	Mn–O18.1–P7.2	4	3.6366	3.66196	0.00064313	
	Mn–O18.1–P7.2–O18.1	2	3.6645	3.68986	0.00064313	
	Mn–O16.1–P7.1–O16.1	2	3.6817	3.70706	0.00064313	
	Mn– O19.1–P12.1–O19.1	2	3.6887	3.71406	0.00064313	
	Mn–O18.1–O16.1	12	3.7103	3.73566	0.00064313	
	Mn–O16.1–O19.1	8	3.7704	3.79576	0.00064313	
	Mn–O27.1	2	3.8089	3.83426	0.00064313	
	Mn–N2.1	2	3.9888	4.01416	0.00064313	
	Mn–C3.1	4	4.0422	4.06756	0.00064313	
	Mn–O20.1	2	4.0482	4.07356	0.00064313	

N corresponds to the degeneracy of scattering paths at each specific interatomic distance. The root mean square error (RMSE) was calculated and presented as well

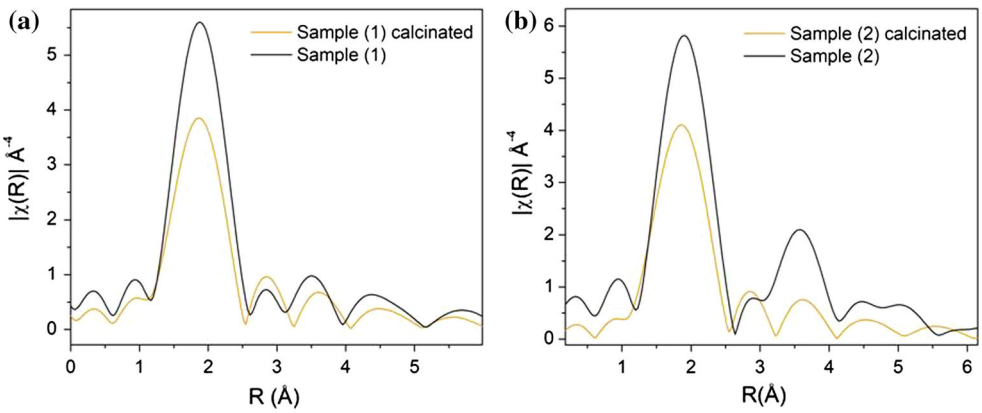

Figure 7 EXAFS spectra before and after calcination of both samples: **a** $MnNP_3$ (**1**) and **b** $Mn(NP_2AH)_2$ (**2**).

Conclusions

Two divalent manganese(II) aminophosphonates were synthesized by liquid-assisted grinding from manganese(II) acetate tetrahydrate and the corresponding phosphonic acids. The products were characterized by PXRD, and the structure of the novel compound $Mn(NP_2AH)_2$ was solved from powder diffraction data. In situ XRD studies showed that the formation pathway of both manganese(II) phosphonates passes through a non-crystalline phase. The potential of both materials for catalyzing the oxygen evolution reaction was tested leading to promising results. The catalytic performance of the manganese

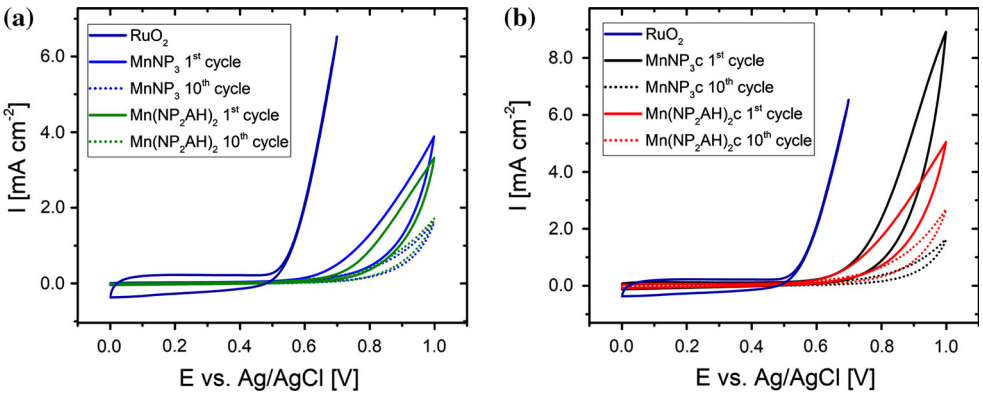

Figure 8 **a** CV curves of uncalcinated samples. **b** CV curves of calcinated samples.

phosphonates could be improved by previous thermal treatment. By calcination, several structural changes in the material are induced. The EXAFS spectra indicate that the coordination number of the Mn atoms decreases, providing new binding sites for the reactants. Furthermore, the single atoms are pre-ordered in the metal phosphonate. This pre-order is assumed to be maintained in the calcined species. As a result, a highly dispersed material is generated. In addition, the calcination process leads to a reduction in the particle size, and therefore, the calcined material can have properties different from the bulk. The structure determination of the calcinated species is subject of ongoing investigations.

Electronic supplementary material: The online version of this article (https://doi.org/10.1007/s10853-018-2608-6) contains supplementary material, which is available to authorized users.

References

[1] Coxall RA, Harris SG, Henderson DK, Parsons S, Tasker PA, Winpenny REP (2000) Inter-ligand reactions: in situ formation of new polydentate ligands. J Chem Soc, Dalton Trans 14:2349–2356. https://doi.org/10.1039/B001404O

[2] Gholivand K, Yaghoubi R, Farrokhi A, Khoddami S (2016) Two new supramolecular metal diphosphonates: synthesis, characterization, crystal structure and inhibiting effects on metallic corrosion. J Solid State Chem 243:23–30. https://doi.org/10.1016/j.jssc.2016.07.027

[3] Kohler C, Rentschler E (2016) Functionalized phosphonates as building units for multi-dimensional homo- and heterometallic 3*d*–4*f* inorganic–organic hybrid-materials. Dalton Trans 45(32):12854–12861. https://doi.org/10.1039/c6dt02023b

[4] Deng M, Liu X, Zheng Q, Chen Z, Fang C, Yue B, He H (2013) Controllable preparation and structures of two zinc phosphonocarboxylate frameworks with MER and RHO zeolitic topologies. CrystEngComm 15(35):7056–7061. https://doi.org/10.1039/C3CE40673C

[5] Ma T-Y, Lin X-Z, Zhang X-J, Yuan Z-Y (2010) High surface area titanium phosphonate materials with hierarchical porosity for multi-phase adsorption. New J Chem 34(6):1209–1216. https://doi.org/10.1039/B9NJ00775J

[6] Brunet E, Alhendawi HMH, Cerro C, de la Mata MJ, Juanes O, Rodríguez-Ubis JC (2010) Easy γ-to-α transformation of zirconium phosphate/polyphenylphosphonate salts: porosity and hydrogen physisorption. Chem Eng J 158(2):333–344. https://doi.org/10.1016/j.cej.2010.01.040

[7] Pili S, Argent SP, Morris CG, Rought P, García-Sakai V, Silverwood IP, Easun TL, Li M, Warren MR, Murray CA, Tang CC, Yang S, Schröder M (2016) Proton conduction in a phosphonate-based metal-organic framework mediated by intrinsic "free diffusion inside a sphere". J Am Chem Soc 138(20):6352–6355. https://doi.org/10.1021/jacs.6b02194

[8] Bazaga-García M, Papadaki M, Colodrero RMP, Olivera-Pastor P, Losilla ER, Nieto-Ortega B, Aranda MÁG, Choquesillo-Lazarte D, Cabeza A, Demadis KD (2015) Tuning proton conductivity in alkali metal phosphonocarboxylates by cation size-induced and water-facilitated proton transfer pathways. Chem Mater 27(2):424–435. https://doi.org/10.1021/cm502716e

[9] Sen R, Saha D, Mal D, Brandão P, Rogez G, Lin Z (2013) Synthesis, structural aspects and catalytic performance of a tetrahedral cobalt phosphonate framework. Eur J Inorg Chem 28:5020–5026. https://doi.org/10.1002/ejic.201300639

[10] Zhao H, Yuan ZY (2017) Transition metal-phosphorus-based materials for electrocatalytic energy conversion reactions. Catal Sci Technol 7(2):330–347. https://doi.org/10.1039/c6cy01719c

[11] Feng PJ, Cheng X, Li JT, Luo XT (2018) Co-3(PO4)(2) nanoparticles embedded in nitrogen-doped carbon as an

advanced electrocatalyst for OER in alkaline solution. Catal Lett 148(1):214–219. https://doi.org/10.1007/s10562-017-2251-x

[12] Feng PJ, Cheng X, Li JT, Luo XT (2018) Calcined nickel–cobalt mixed metal phosphonate with efficient electrocatalytic activity for oxygen evolution reaction. ChemistrySelect 3(2):760–764. https://doi.org/10.1002/slct.201702637

[13] Clearfield A (1998) Metal phosphonate chemistry. In: Karlin KD (ed) Progress in inorganic chemistry, vol 47. Wiley, New York, pp 371–510

[14] Friscic T, Halasz I, Beldon PJ, Belenguer AM, Adams F, Kimber SA, Honkimaki V, Dinnebier RE (2013) Real-time and in situ monitoring of mechanochemical milling reactions. Nat Chem 5(1):66–73. https://doi.org/10.1038/nchem.1505

[15] Gracin D, Štrukil V, Friščić T, Halasz I, Užarević K (2014) Laboratory real-time and in situ monitoring of mechanochemical milling reactions by raman spectroscopy. Angew Chem Int Ed 53(24):6193–6197. https://doi.org/10.1002/anie.201402334

[16] Batzdorf L, Fischer F, Wilke M, Wenzel KJ, Emmerling F (2015) Direct in situ investigation of milling reactions using combined X-ray diffraction and raman spectroscopy. Angew Chem Int Ed 54(6):1799–1802. https://doi.org/10.1002/anie.201409834

[17] Cabeza A, Ouyang X, Krishnamohan Sharma CV, Aranda MAG, Bruque S, Clearfield A (2002) Complexes formed between nitrilotris(methylenephosphonic acid) and M^{2+} transition metals: isostructural organic–inorganic hybrids. Inorg Chem 41:2325–2333. https://doi.org/10.1021/ic0110373

[18] Topas Version 5 (2014). Bruker AXS

[19] David WIF, Shankland K, van de Streek J, Pidcock E, Motherwell WDS, Cole JC (2006) DASH: a program for crystal structure determination from powder diffraction data. J Appl Crystallogr 39(6):910–915. https://doi.org/10.1107/S0021889806042117

[20] Riesemeier H, Ecker K, Görner W, Müller BR, Radtke M, Krumrey M (2005) Layout and first XRF applications of the BAMline at BESSY II. X-Ray Spectrom 34(2):160–163. https://doi.org/10.1002/xrs.750

[21] Ravel B, Newville M (2005) ATHENA, ARTEMIS, HEPHAESTUS: data analysis for X-ray absorption spectroscopy using IFEFFIT. J Synchrotron Radiat 12(4):537–541. https://doi.org/10.1107/S0909049505012719

[22] Guan L, Wang Y (2015) Hydrothermal synthesis, crystal structure and properties of a novel chain coordination polymer constructed by tetrafunctional phosphonate anions and cobalt ions. J Solid State Chem 228:9–13. https://doi.org/10.1016/j.jssc.2015.04.008

[23] Melder J, Kwong WL, Shevela D, Messinger J, Kurz P (2017) Electrocatalytic water oxidation by MnOx/C. In situ catalyst formation, carbon substrate variations, and direct O_2/CO_2 monitoring by membrane-inlet mass spectrometry. Chemsuschem 10(22):4491–4502. https://doi.org/10.1002/cssc.201701383